Effect of spacer configuration on hydraulic conditions using PIV

Haidari, A. H.; Heijman, S. G.J.; van der Meer, W. G.J.

DOI
10.1016/j.seppur.2018.01.022

Publication date
2018

Document Version
Final published version

Published in
Separation and Purification Technology

Separation and Purification Technology 199 (2018) 9–19

Contents lists available at ScienceDirect

Separation and Purification Technology

journal homepage: www.elsevier.com/locate/seppur

Effect of spacer configuration on hydraulic conditions using PIV

A.H. Haidari[a,*], S.G.J. Heijman[a], W.G.J. van der Meer[a,b,c]

[a] Delft University of Technology, Department of Civil Engineering, Stevinweg 01, 2628 CN Delft, The Netherlands
[b] Oasen, P.O. Box 122, 2800 AC Gouda, The Netherlands
[c] University of Twente, Faculty of Science and Technology, Drienerlolaan 5, 7522 NB Enschede, The Netherlands

ARTICLE INFO

Keywords:
Feed spacer
Membrane
Particle Image Velocimetry
PIV
Spiral wound modules
Reverse osmosis

ABSTRACT

Making improvements to feed spacers of spiral-wound membrane (SWM) modules of reverse osmosis (RO) is a necessary step towards a wider application of these modules. This study sets out to evaluate the performance of six commercial feed spacers by comparing their actual velocity profiles and their pressure drop. Velocity profiles are obtained from Particle Image Velocimetry (PIV). Comparing images from PIV with corresponding friction losses revealed that the transition from steady to unsteady flow occurs at the moment when the incline of the friction factor changes from steep to slight. From the two types of spacers used, zigzag spacers showed a better distribution of flow than the cavity spacers did, but at the cost of higher pressure drop. The flow was in a straight line from inlet to outlet with zigzag spacers only at low Reynolds numbers and with cavity spacers for the entire studied range of Reynolds numbers. Additionally, results showed that hydraulic conditions in channels with cavity spacers are mainly affected by geometric characteristics of transverse filaments. The results from this study can be used to understand the effects of spacer geometry on the hydraulic conditions inside the feed channel and as a validation tool for computational modeling.

1. Introduction

Safe and clean water is in short supply in many corners of the globe. Reverse osmosis (RO) is a popular desalination technique, which has been employed to satisfy the ever-growing demand for water for municipal and industrial consumption. Aside from desalination, there is likely to be a growing trend towards the use of RO for purification of fresh water from rivers, canals, and faucets, because RO can provide an excellent barrier against micro- and nano-contaminants. Dealing with emerging micro- and nano-pollutants remains a continuing challenge for treatment plants, because these pollutants are often dangerous even at low concentrations and cannot (easily) be removed from the feed water with conventional techniques [1]. For instance, Wong et al. [2] have reported that certain species are in danger of extinction in almost half of European and North American rivers and lakes because of the pollution of these ecosystems [1].

A wider application of RO is possible by bringing down the unit costs of water production in these membranes. Considering the worldwide water production by RO (74.4 million m^3 in 2015) [3], high energy costs, and the fact that spiral-wound membrane (SWM) modules are the most popular commercial configuration of RO [4], the costs of RO systems can be significantly reduced even by small improvements in the efficiency of these modules. Improvements in SWM modules can be achieved by modification of important pieces of a membrane module such as the number and size of envelopes [5,6], the physical and chemical properties of membrane material, and adapting the spacers' configuration. Spacers are inexpensive parts in an SWM module, which are used to prevent membrane surfaces from touching each other; they thereby provide permeate and feed flow paths (channels). The feed spacer also facilitates mixing between the bulk of fluid and the fluid adjacent to the membrane surface [7]; it thereby minimizes the effects of concentration polarization. The latter has been considered to be the primary function of feed spacers, since feed spacers in RO were historically designed to prevent concentration polarization in seawater modules.

A slight increase in feed spacer thickness (from 28 to 34 mils) is one of the few changes that feed spacers of RO have undergone. A proper design of a feed spacer for new applications would be possible through the investigation of hydraulic conditions in SWM modules. The hydraulic conditions of SWM modules can be investigated through performing numerical and experimental studies on the pressure drop and velocity development inside spacer-filled channels. For instance, effects of the ratio of filament length to channel height (l_m/H_{CH}), flow attack angle (α), and hydrodynamic angle (β) have been subjects of many numerical and experimental studies related to spacer performance [8–17].

* Corresponding author at: Room S3.02.020, Stevinweg 01 (Building 23 = Civil Engineering Faculty of Delft University of Technology), 2628 CN Delft, The Netherlands.
E-mail address: a.h.haidari@tudelft.nl (A.H. Haidari).

https://doi.org/10.1016/j.seppur.2018.01.022
Received 10 November 2017; Received in revised form 10 January 2018; Accepted 10 January 2018
Available online 11 January 2018

Nomenclature

A	the cross-section area of the feed channel [m^2]
A_{CT}	filaments' cross-section area parallel to flow [m^2]
A_{CP}	filaments' cross-section area perpendicular to flow [m^2]
A', n	constants in the friction factor dependency on Reynolds number [Depending on each other]
A_{eff}	the cross-section area of the feed channel involving the spacer porosity [m^2]
C_{td}	Darcy-Weisbach factor, Manning friction factor, or total drag
$d_{f1} = d_{f\_CP}$	thickness of filament of spacer in parallel direction to the flow [m]
$d_{f2} = d_{f\_CT}$	thickness of filament of spacer in perpendicular direction to the flow [m]
d_h	hydraulic diameter [m]
Δp	pressure drop [pa]
h_{sp}	thickness of feed spacer [m]
H_{CH}	height of feed channel [m]
K, m	constants in the pressure drop dependency on velocity [Depending on each other]
L	Length of feed channel [m]
l_m	mesh length of spacer in direction parallel/perpendicular to flow [m]
$l_{m1} = l_{m\_CP}$	mesh length of spacer in direction parallel to flow [m]
$l_{m2} = l_{m\_CT}$	mesh length of spacer in direction perpendicular to flow [m]
Q	Flow [m^3/s]
Re	Reynolds number
Re_h	hydraulic Reynolds number
$S_{v,sp}$	specific surface of the spacer [1/m]
U_{aver}	average velocity [m/s]
U_{sup}	superficial velocity [m/s]
V_{sp}	volume of spacer in a mesh [m^3]
V_{mesh}	total volume of a mesh [m^3]
W	width of feed channel [m]
X	flow direction
Y	direction perpendicular to flow but not in the direction of channel height
Z	direction perpendicular to flow and in the direction of the channel height
Z1	plane close to the membrane surface
Z2	plane close to the middle of the feed channel at the boundary of top and bottom filaments
Z3	Plane close to Plexiglas surface or close to observation window

Greek symbols

α	spacer's flow attack angle [degree]
β	spacer's angle or hydrodynamic angle of spacer [degree]
ε	porosity of spacer filled-channel [-]
μ	dynamic viscosity of the fluid [kg/(m.s)]
ρ	density of the water [kg/m^3]

Abbreviation

PIV	Particle Image Velocimetry
RO	Reverse Osmosis
SWM	Spiral-wound membrane

Numerical studies have made a great contribution to a better understanding of spacer performance. In this context, Schwinge et al. [18] and Fimbres and Wiley [19] contributed comprehensive overviews. While in many numerical calculations spacers with a simplified filament cross-section are used, the experimental data with commercial feed spacers [6,20–22] have shown that detailed characteristics of filaments are essential for determining flow conditions in spacer-filled channels. For instance, Neal et al. [22] showed that the precipitation of particles is influenced by the shape of filaments in commercial spacers. They [22] observed that particle deposition mostly occurs around the point where the attached filaments bulge outward. In this light, some researchers [23,24] have started to use spacers with closer geometrical similarities to those of commercial spacers for the numerical studies. Additionally, while numerical studies are able to provide detailed information on velocity profiles, they are usually validated with low-resolution experimental studies because of a limited number of direct experimental studies on the detailed velocity profiles [19,25].

Particle Image Velocimetry (PIV) is a non-invasive technique for measurement and visualization of the flow with high resolution. Results of PIV are instantaneous velocity maps, which can be averaged over time. The velocity maps can be used to determine the state of flow, identify the low and high velocity areas and dead zones, determine the flow distribution, etc. However, to the authors' knowledge, there are only limited studies done with PIV in the field of membrane technology.

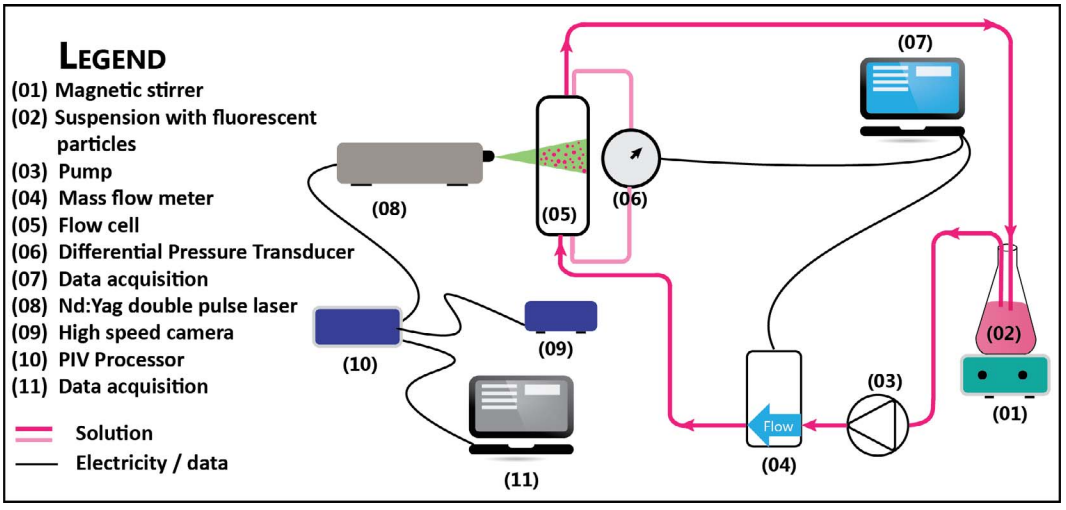

Fig. 1. The experimental setup used for measurement of the pressure losses over the flow cell (05) and for visualization of the temporal and spatial velocity variations inside the spacer-filled channel [28].

Gaucher et al. [26] made use of PIV for visualization of the flow in ultrafiltration flow cells without a spacer. The flow in their experiment [26] was from inlet to outlet in a straight line with small deviations around the inlet and outlet. They [26] found a lower average velocity with PIV than the expected average velocity. Gimmelshtein and Semiat [27] and Willems et al. [25] used the PIV technique to visualize the flow inside spacer-filled channels. Gimmelshtein and Semiat [27] reported that the flow was from the inlet to the outlet in a straight line while Willems et al. [25] indicated that flow was along the attached filaments at the corresponding channel heights. The difference between the results of these two studies was the consequence of using different setups. Gimmelshtein and Semiat [27] used a spacer thinner than the channel height [25] and due to this, a space was created above the spacer in which the flow was in a straight line. Willems et al. [25] used spacers with thicknesses the same as channel heights. In a previous study [28], we compared the flow inside an empty channel with that of a spacer-filled channel by using the PIV technique. The results showed that the flow was in a straight line from inlet to outlet in the empty channel, thus in agreement with the results of Gaucher et al. [26], and it was along the filament at the corresponding height in the spacer-filled channel, thus in agreement with the results of Willems et al. [25]. This indicates that the camera in the study done by Gimmelshtein and Semiat [27] was probably focused on the empty part of the feed channel.

The purpose of this study is to compare commercial spacers of different configuration by using PIV and measuring the pressure drop along their flow channel. In this context, velocity profiles with high resolution will be provided without any simplification to geometric characteristics of spacers. First, the setup and the measurement method are explained. Then, pressure losses and friction factors are illustrated for examined spacers. Next, variations in simultaneous velocity profiles are revealed for particular points from the field of view. After that, the averaged spatial velocity map is discussed for a specific flow and then for the entire range of flows. Finally, PIV results at which the friction factor shows extreme changes are illustrated for one of the spacers.

2. Experimental

Fig. 1 illustrates a schematic view of the experimental setup used in this study. A solution (02) containing fluorescent particles is circulated through a mass flow meter (04) and then a flow cell (05) by means of a pump (03) to the feed tank. The pressure drop over the flow cell is measured by means of a differential pressure transducer (06). Values from the pressure transmitter are used to calculate the friction losses. Simultaneously, velocities are measured when a laser (08) emits two light pulses and a high-speed camera (09) takes two images (11) within a short time interval. The captured images are used to determine the temporal and spatial velocity maps using a commercial software application called Davis 7.2. A detailed description of instruments and the setup can be found in a previous study [28].

Measurements were taken inside an embedded flow channel (L = 200 mm and W = 40 mm) in a flat flow cell (L = 260 mm, W = 85 mm, H = 55 mm). The flat flow cell may be used in these types of experiments because feed channels in SWM modules are small enough to ignore the curvature effects of these modules on the flow [9,12]. Together with spacers, a membrane coupon (Trisep-AMC1) was placed inside the embedded flow channel. Plastic shims were used to adjust the channel height according to the spacer thickness in such a way that the channel's height was equal to the spacer's thickness. The experiments were conducted without the permeate production, because the ratio of permeate is small compared to the cross-flow velocity in RO. The non-woven commercial feed spacers (DelStar Technologies, INC.) were made of polypropylene without any further modifications. The studied spacers are shown in Fig. 2, and their geometric specifications are given in Table 1.

Spacers A, B, C, and D are called zigzag spacers in this article and spacers G and H are called cavity spacers. Spacers A, B, and C are mostly applied in manufacturing of commercial SWM modules of RO, and spacers G and H in ultrafiltration. Spacers G and H are used to compare the possible occurrence of fouling patterns in cavity spacers compared to zigzag spacer, through studying the velocity changes in time and place. The authors could not find any RO elements with spacer D. Filaments of zigzag spacers had an almost circular cross-section with a variable diameter along each filament in a mesh [28]. Filaments of cavity spacers had a rectangular or an oval cross-section rather than a circular form. The geometrical characteristics of spacers mentioned in Table 1 are the average of at least ten measurements in the laboratory. There are slight differences between these values and values provided by the manufacturer. These differences arose from the fact that manufacturers count the numbers of meshes in one inch, while we measured the pitch length of mesh(es). In the former, the starting point of the measurement could be the center of a filament and the ending point the middle of one of the subsequent meshes.

Table 1 shows that the ratio of filament thickness to the channel height (relative height) is higher than 0.5 in all cases of zigzag spacers. That is in contradictory with most numerical studies that assume a relative height of 0.5. Each filament thickness mentioned in Table 1 is an average of 10 measurement points over the length of a filament in a mesh. The porosity and hydraulic diameter (Table 1) are respectively calculated using Eq. (1) [21] and Eq. (2) [19,21].

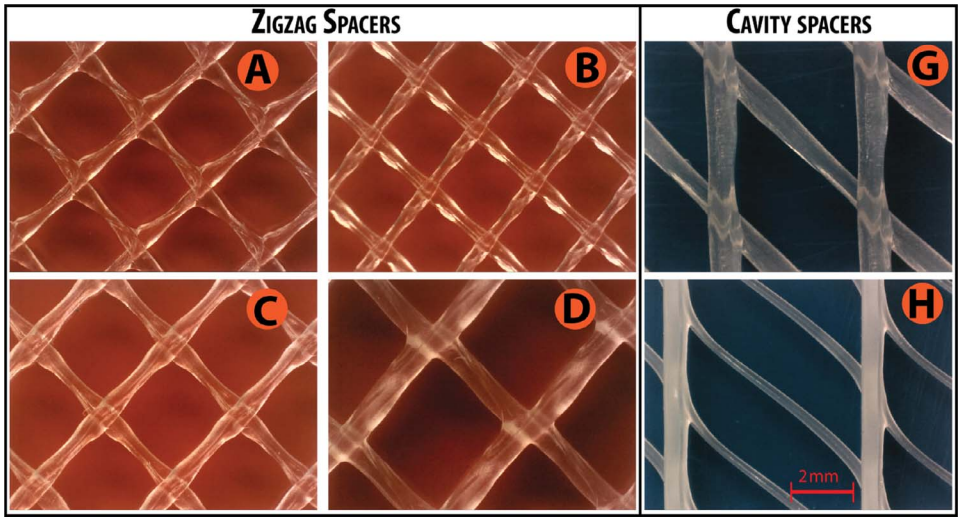

Fig. 2. The feed spacers are categorized into two configurations: zigzag spacers (spacers A-D) and cavity spacers (spacers G and H). All spacers used in this study are provided by the DelStar Technologies.

Table 1
Structure properties of feed spacers used in this study. The spacers are categorized into the zigzag spacers (A–D) and the cavity spacers (G and H). (Please also see item mentioned in Fig. 3C).

Description	Nomenclature		Zigzag spacers				Cavity spacers	
	Symbol	Unit	A	B	C	D	G	H
Spacer/channel height	hSP = HCH	10^{-3} m	0.71	0.76	0.86	1.22	1.15	1.25
Filament diameter parallel to flow	df1 = df_CP	10^{-3} m	0.39	0.45	0.49	0.8	0.65 × 0.92	1.01 × 0.58
Filament diameter perpendicular to flow	df2 = df_CT	10^{-3} m	0.39	0.45	0.49	0.8	0.50 × 0.81	0.24 × 0.33
Filament length parallel to flow	lm_CP	10^{-3} m	2.85	2.45	3.20	4.41	4.87	3.08
Filament length perpendicular to flow	lm_CT	10^{-3} m	2.85	2.45	3.20	4.41	4.87	6.36
Hydrodynamic angle	β	o	89.5	89	89.2	89.8	45	45
Flow attack angle	α	o	45.5	46	45.8	45.2	135	135
Aspect ratio	lm_CP/HCH	–	4.01	3.21	3.72	3.62	4.23	2.47
Ratio of filament's distance to thickness	lm_CP/df_CT		7.33	5.44	6.53	5.51	6.0–7.5	9.3–12.3
Relative height	df_CT/HCH	–	0.55	0.59	0.56	0.66	0.44–0.70	0.19–0.26
Porosity	ε	%	88	83	88	81	80	82
Hydraulic diameter	dh	10^{-3} m	0.88	0.8	1.08	1.26	1.1	1.21

$$\varepsilon = 1-\frac{V_{sp}}{V_{mesh}} = 1-\frac{\frac{1}{2}(2.\,A_{CT}.\,l_{m.CT} + 2.\,A_{CP}.\,l_{m.CP})}{(l_{mCT}*l_{m.CP}*\sin(\beta))*H_{CH}} \quad (1)$$

$$d_h = \frac{4\times\varepsilon}{\frac{2}{H_{CH}} + (1-\varepsilon).\,S_{v,SP}} \quad (2)$$

Sv, sp in Eq. (2) represents the specific surface of the feed spacer and is calculated by dividing the feed spacer surface to its volume. A list of other parameters and symbols can be found at the beginning of this article. The state of flow is determined by defining the relation (Eq. (3)) between the pressure drop and the power (m) of average velocity in the main direction of flow (U_{ave}).

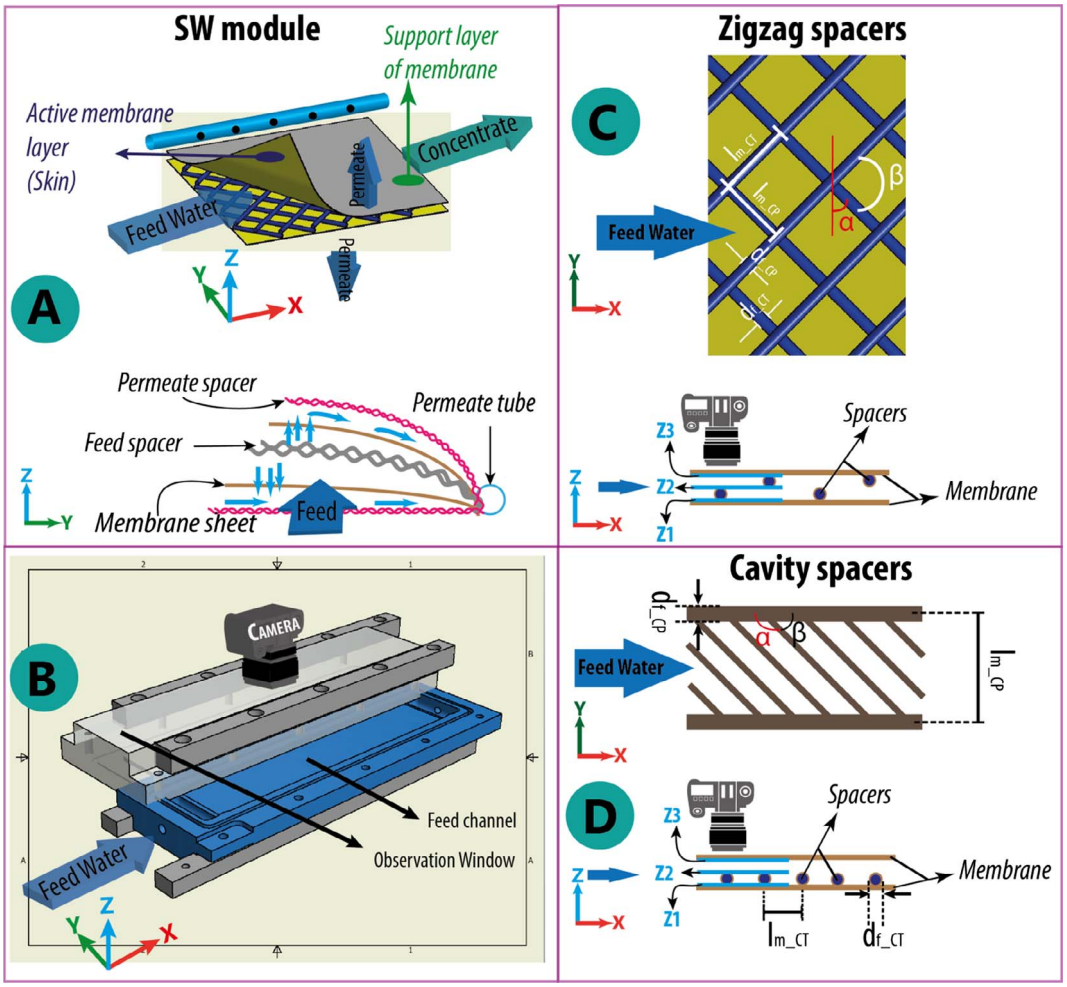

Fig. 3. Each envelope in SWM modules is formed by glueing two flat sheets along their three edges at the non-active side (support layer). In this way, the active layers (skins) of the membrane's sheets face the feed spacer and the support parts of the sheets face the permeate spacer (A). The feed spacer is relatively thicker and more porous than the permeate spacer (A). The schematic view of the flow cell, location of the feed channel, and position of the camera is shown (B). The top and side views of a zigzag spacer (C) and a cavity spacer (D) are shown. The camera is focused at three heights: Z1 (rear part of the channel and close to the membrane coupon), Z2 (middle part of the channel), and Z3 (front part of the channel and close to the observation window) (C, D).

$$\Delta p \propto K \times (U_{ave})^m \tag{3}$$

K is a constant that depends on the spacer and channel's geometry. It was suggested [29,30] that an "m" value around one indicates a laminar flow, and around 1.75 a turbulent flow. However, according to literature, the Reynolds number in SWM modules of RO is much lower than the Reynolds number in the turbulent regime. Therefore, as has been suggested [19,31] it is better to talk about the flow disruption as eddies in SWM modules of RO rather than turbulence.

Eq. (4) is used to calculate the average velocity in the flow direction (U_{ave} Eq. (3)) by considering the porosity of the feed spacer (Eq. (1)), feed channel dimensions (W, H_{CH}), and the feed flow (Q). In some studies [19], the average velocity is referred to as effective velocity.

$$U_{ave} = \frac{U_{sup}}{\varepsilon} = \frac{Q}{A_{eff}} = \frac{Q}{A.\,\varepsilon} = \frac{Q}{W.\,H_{CH}.\,\varepsilon} \tag{4}$$

In some literature, the relation between the Reynolds number (Eq. (6)) and the friction factor (C_{td}) is used (Eq. (5)) to determine the state of flow inside the feed channel.

$$C_{td} \propto \frac{A'}{(Re_h)^n} \tag{5}$$

In Eq. (5), A' is a constant that depends on the spacer and channel's geometry. The term Reynolds number (Eq. (6)) in this study refers to the hydraulic Reynolds number (Re_h), which is in agreement with the definition of the Reynolds number used by Schock and Miquel [6] and Fimbres-Weihs and Wiley [19,32].

$$Re_h = \frac{\rho.\,U_{ave}.\,d_h}{\mu} \tag{6}$$

The hydraulic Reynolds number is determined as a function of the average velocity of the spacer-filled channel (Eq. (4)) and the channel height (H_{CH}). Other typical definitions for Reynolds number used in the literature are the channel Reynolds number [33] and the cylinder Reynolds number [14]. The channel Reynolds number and the cylinder Reynolds number make use of the average velocity in the empty channel (U_{sup} in Eq. (4)) in combination with channel height and filament diameter respectively [19].

The two required frames for determining a velocity field are captured at a known distance (100 mm) from inlet and from channel edges (15 mm) to limit effects of boundaries (entrance, edges and exit) on the flow and to ensure a fully developed flow. The time interval between the two frames was adjusted to the particle displacement in order to reduce the number of pairing losses [28]. The fluorescent particles (tracers) had a mean diameter of 10 µm and a density of 1.19 g/cm^3. The Stokes number for these particles was around 5×10^{-3} for the thinnest spacer used (spacer A), and thus tracing accuracy errors were below 1% [34] in all experiments. The quality of vector maps was improved by using a combination of coated particles with Rhodamine-B, green light laser (wavelength = 545 nm), and an optical filter.

PIV measurements are taken at three different heights in the feed channel separately: close to the camera (Z3), at the middle of the channel (Z2), and far from the camera or close to the membrane sheet at the bottom of the feed channel (Z1) (Fig. 3). The thickness of laser sheet light (2 mm) was greater than the feed channel height (0.71–1.62 mm), and therefore, the entire depth of the channel was illuminated. That is a common situation in µPIV [25] and can be solved by fixing the focus of the camera at a specific distance from the lens and moving the flow cell [25,35]. In this study, the camera was displaced

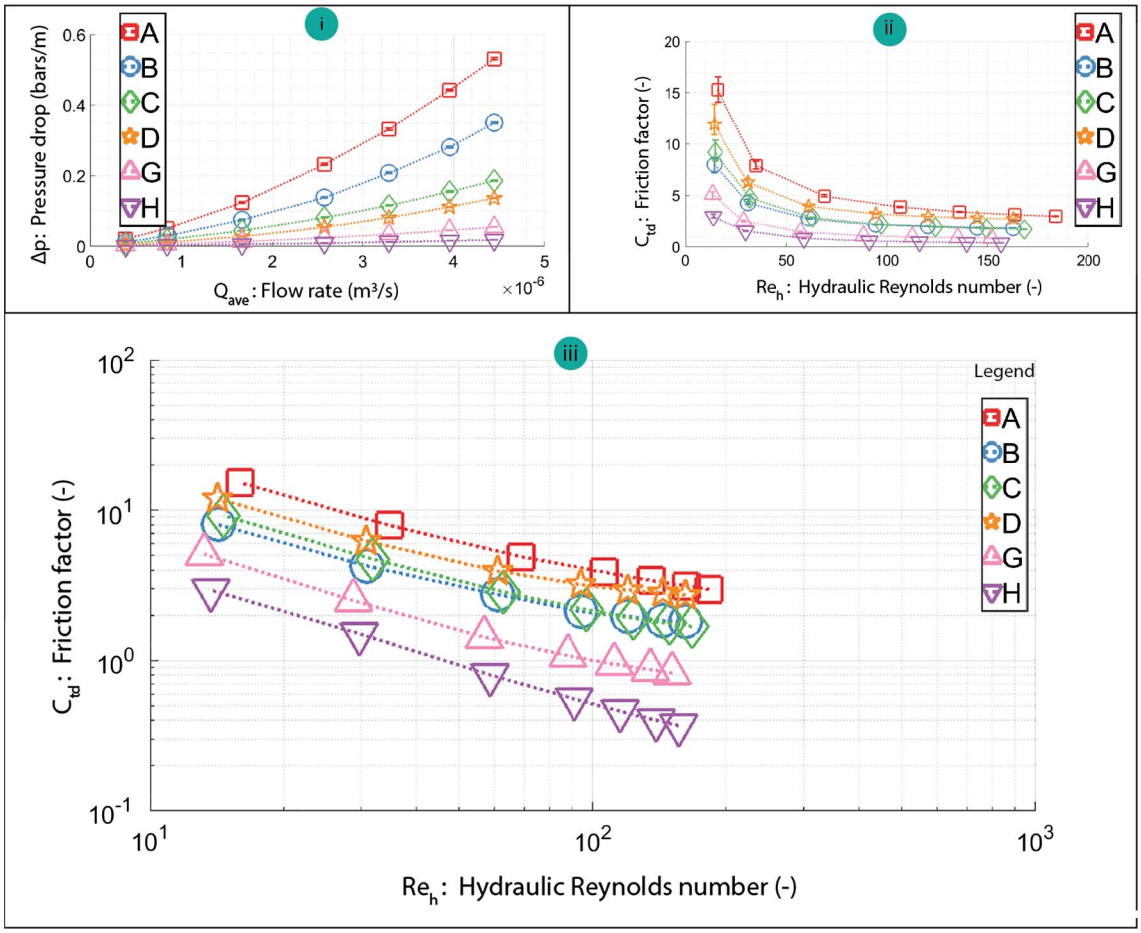

Fig. 4. Development of pressure drop against increasing flow rate (i) and variation of friction factor for increasing hydraulic Reynolds number in a normal view (ii) in logarithmic view (iii).

using a translation stage because moving the flow cell was not possible. The camera was initially arranged in such a way that only particles in the plane close to the camera (Z3 in Fig. 3) were in focus and particles at the middle of the channel (Z2 in Fig. 3) and close to the membrane (Z1 in Fig. 3) were barely in focus. The camera was then moved in steps of 50 μm to the subsequent positions (Z1 and Z2) using the translation stage. The camera's depth of field was about 0.14 mm. At each depth, 50 pairs of images (100 frames) were taken for a specific flow rate. An instantaneous (momentary) velocity map is calculated from each pair of successive frames. These 50 instantaneous velocity maps are used to analyze variations of velocity in time (temporal velocity). An average velocity map (averaged spatial velocity profile) is calculated from the 50 momentary velocity profiles and is used to study the spatial velocity inside the feed channel [28].

3. Results and discussions

3.1. Pressure drop and friction factor

Fig. 4 illustrates variations of pressure drop against the increasing flow rate (A) and the variation of friction losses against Reynolds number in the normal (B) and logarithmic (C) view. Each line in Fig. 4 demonstrates a spacer wherein each point is the average of at least 450 measurements, which are performed parallel to the PIV measurements.

Pressure drop and friction losses are important in the design of a spacer because they are related to the additional energy cost in SWM modules. Fig. 4A shows that the pressure drop increases by increasing the flow rate in each spacer and by the decrease in the channel height for a particular flow. Additionally, Fig. 4A shows that differences between pressure drop values of different spacers are greater at a higher flow rate. The pressure drop in zigzag spacers (spacers A, B, C, and D with an approximate $\beta = 90°$) was higher than the cavity spacers (spacer G and H with an approximate $\beta = 45°$) even when the channel height of the zigzag spacer (spacer D) was approximately the same as with cavity spacers. That is due to the size of transverse filaments, their distance from each other, and the specific orientation of these filaments in cavity spacers.

Da Costa et al. [21] showed that there is a relation between the pressure drop and the aspect ratio (l_{m_CT}/H_{CH}). The result from our study indicates that the pressure drop increase was consistent with the decrease of the aspect ratio (l_{m_CT}/H_{CH}) in cavity spacers but not in the zigzag spacers. Spacer C is the exception in our experiment, which has a smaller ratio of l_{m_CT}/H_{CH} than spacer D but also a lower pressure drop.

Fig. 4B shows that the friction factor is remarkably lower in the cavity spacers than in the zigzag spacers. In a numerical simulation, Koutsou et al. [13] investigated the effects of spacer geometry on the pressure drop. They used dimensionless pressure drop, which was related to a friction coefficient. They found that the pressure drop in zigzag spacers increased at a smaller ratio of the filament's distance to the filament's diameter (l_m/d_f) independently of the hydrodynamic angle. Their result was in agreement with similar previous studies [6,8,15,21,36,37]. The results from our study showed that decrease of the friction factor was inconsistent in spacer C with respect to the increase of the l_m/d_f ratio. This inconsistency arose because commercial spacers are different in more characteristics than just the l_m/d_f ratio. For instance, Koutsou et al. [13] mentioned that there were exceptions when the ratio of l_m/d_f is combined with the hydrodynamic angle of spacer (β), which is also the case in our experiment (Table 1). In addition, filaments in commercial spacers are not perfectly circular in shape, and their diameters are not uniform and equal over the filaments' length, as is usually assumed in numerical studies. Therefore, it is difficult to draw a general conclusion based only on the presented data.

Fig. 4B shows that friction factor curves against the Reynolds number have the shape of a decreasing power equation, as was expected according to Eq. (5) ($C_{td} = A'/Re^n$). Former studies [13,21,37] have illustrated decreasing linear lines, which are in agreement with the tail part of the curves in this study ($Re_h > 100$). The changing pattern of the friction factor from descent with steep incline to descent with slight incline in these curves ($30 < Re_h < 90$) is the moment that mixing of flow was extremely enhanced and might be the moment that flow conditions change from steady to unsteady flow. This issue will be discussed in more detail and with consideration of the PIV images in Section 3.2.3.

Fig. 4C represents the logarithmic view of Fig. 4B. Except spacer H, other spacers show a breakpoint in the friction factor lines at a Reynolds number close to 90. i.e. the lines at $Re_h > 90$, except spacer H, become less steep indicating a higher unsteadiness with these spacers. These results are based only on the friction factor calculation and measurement of the pressure drop. More visual evidence will be provided by the PIV images at Section 3.2.3.

3.2. Actual velocity measurements with PIV

This section includes velocity maps obtained from PIV. The camera's field of view (approximately H = 7.5 mm × W = 9.5 mm) is the same in all velocity maps presented in the next sections.

3.2.1. Temporal velocity profiles

In PIV, a momentary velocity map is shaped by determining the shifting distance of particles between two frames at a particular time interval (Fig. 5). Fifty momentary velocity profiles are made for a

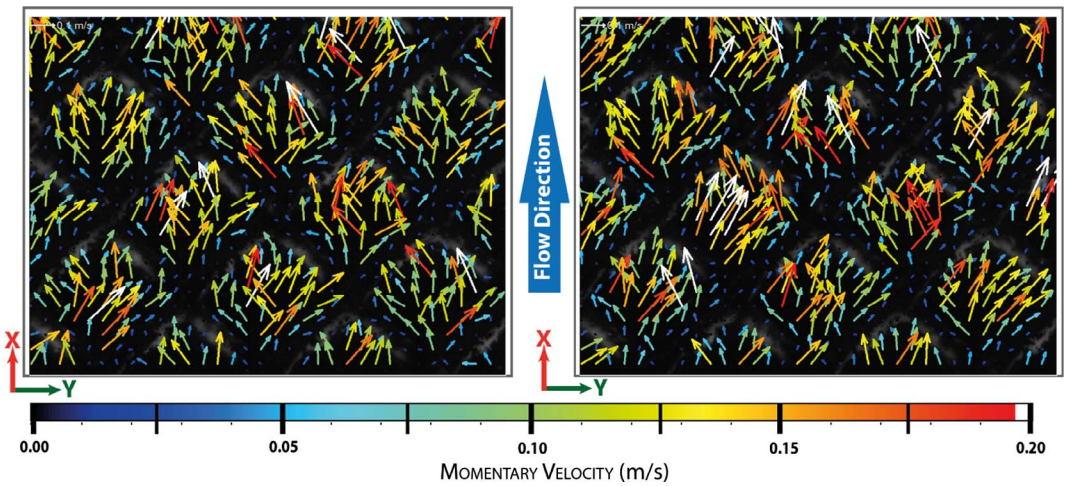

Fig. 5. Two momentary velocity profiles of spacer B at the middle of channel (Z2 in Fig. 3D) for an average velocity of about 0.1 m/s (Re = 95).

particular flow of a spacer at each channel height.

Fig. 6 illustrates variations of normalized velocity ($U_{meaured\_in\_E}/U_{ave}$) along the 50 instantaneous velocity profiles for point E, which is located in the middle of one of the meshes in the field of view; i.e., point E has the same XY-coordinates but different Z-coordinates (Z1, Z2, and Z3 in Fig. 3D). The circles and horizontal lines inside each box denote the mean and median of the data respectively, and the filled circles outside the boxes represent the outliers. A normalized velocity is used because the magnitude of velocity was not the same in all spacers. The position of the mean and the median with respect to each other describe the behavior of flow at the studied point. For instance, when the mean is smaller than the median, the data symbolize a left-skewed normal distribution in which momentary velocities with a higher magnitude occur more frequently at the studied point, and therefore, a higher shear applied more frequently at point E for a specific spacer. According to this, higher shear occurs more frequently in the middle of the meshes of spacer C and H at all three channel heights (Fig. 6). However, spacer H has a considerably lower velocity than expected at the membrane side where transverse filaments touch the membrane coupon.

In most studied spacers (Fig. 6), the normalized velocity shows a value around one or higher. This indicates that the measured average velocity is about the same as or higher than the average velocity at point E. Spacers B, C, and G show a normalized velocity greater than one in all three channel heights at point E.

Fig. 6 shows that there is probably a relation between the spacer thickness (channel height) and velocity variations in a channel. A greater channel height will probably result in a stronger vortex shedding at point E. Velocity variation in time could be related to the fouling and concentration polarization. In zigzag spacers, the velocity variation increases by the increase of the channel height at the observation window and the membrane side. At the middle of the channel, however, it decreases with increase of channel height until spacer C and then increases in spacer D. The velocity variation in cavity spacers is almost the same in both spacers because they have approximately the same channel heights. The latter indicates that the velocity variation depends on the channel height rather than the transverse filaments' thickness.

Spacer C has the highest relative discrepancy between the variation of velocity at the middle of the channel (Z2) and membrane sides (Z1 and Z3). It is desirable to have velocity with low variations in the middle of the channel and velocity with high variations at the membrane sides when designing a feed spacer, because this situation can reduce the chance of fouling formation with the lowest possible energy losses.

In cavity spacers, the average velocity is lower on the channel side that the transverse filaments are attached to (Z1) than the side without transverse filaments (Z3). The average velocity of spacer H at Z1 is notably lower than other spacers. The transverse filaments in spacer H are thinner than longitudinal filaments, and the ratio of l_{m_CP}/H_{CH} is smaller in this spacer than in other spacers.

3.2.2. Averaged spatial velocity profiles at $U_{ave} = 0.1$ m/s

The results from the previous section discussed only one point of velocity maps. To investigate how velocity changes spatially, the 50 momentary velocity fields were averaged into one velocity map at each channel height and for a particular flow (Fig. 7).

In the zigzag spacers, the flow direction at Z1 is perpendicular to Z3 and along the filaments at the corresponding heights. The velocity profiles at the middle of the channel (Z2) are the mix of the velocity profiles at Z1 and Z3. These results are in agreement with results obtained by Willems et al. [25].

As shown in Fig. 7, the location of the highest and lowest velocity differs in each spacer at the specific channel height. In the zigzag spacers, the highest velocity occurs near the mesh entrance where water passes over or under a filament, i.e. the areas with high-velocity values at Z1 and Z3. More specifically, the highest velocity occurs when water passes over a filament at the entrance of a mesh and under the adjacent outlet filament (shortest route). The lowest velocity in a mesh occurs close to the inner angle of the downstream node.

Fig. 7 also illustrates that the flow is in an almost straight line from the inlet to the outlet and parallel to longitudinal filaments in the cavity spacers. In addition, the velocity magnitude is much lower at the side of a mesh where transverse filaments are attached to the membrane.

The flow disruption is greater in spacer G than spacer H, because transverse filaments are larger in spacer G. Additionally, Fig. 7 shows that the highest velocity occurs over the transverse filaments with spacer G and at a short distance behind transverse filaments, with a low-velocity zone in between with spacer H.

3.2.3. Averaged spatial velocity at increasing flow rate

Fig. 8 shows the development of averaged spatial velocity for the entire range of flow rates at the middle of the channel. Each plotted box corresponds to a particular flow rate in a spacer. As expected, the variation and the averaged value of measured velocity (Fig. 8) increased by increasing of the flow rate with each spacer. Additionally, the average velocity and the velocity variation decrease with an increase in channel height at a particular flow in both types of spacers.

Notably, in all spacers there are velocities very close to zero for the whole range of flow rate, indicating the existence of dead zones in all spacers and for all applied flows. In all cases, the lower whisker is smaller than the upper whisker, indicating a greater variation in higher velocity ranges. In most cases, except for spacer B at Q = 16 L/h, the position of first quartile becomes higher with the increase of flow, indicating the shift of main flow to higher velocity values. The exception in spacer B might be due to the low ratio of l_{m_CP}/H_{CH} in this spacer and the creation of more dead zones at higher flow rates. The latter indicates that there is an optimal flow rate for each spacer. However, more experiments are required to confirm this.

In zigzag spacers, interestingly, the greatest difference between boxes occurs at the flow transition from Q = 6 L/h to 9 L/h. This is the area in which the incline in friction factor curves changes from descent steep to descent slight ($30 < Re_h < 95$ in Fig. 4B). Fig. 9 visualizes the development of the flow pattern for spacer B at $30 < Re_h < 95$ at the three heights of the channel when the incline of the friction factor curve changes suddenly in this spacer. At $Re_h = 30$ the velocity is in a straight line from the inlet to the outlet at all three heights. By increasing the Re_h to 60, the flow direction at the top and the bottom of the channel changes along the filament's direction, but the flow in the middle of the channel remains in a straight line from inlet to outlet. By further increasing the Re_h to 95, the flow at the middle of the channel starts to show the mixing pattern as discussed in the previous studies [25] and in the previous sections of this study (Fig. 7).

The phenomenon described above was also observed in other

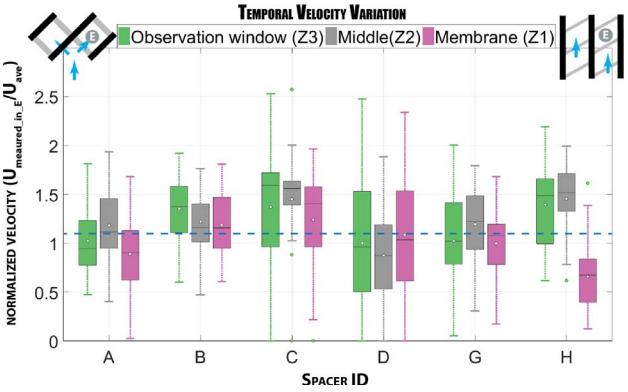

Fig. 6. Variations of normalized velocity ($U_{meaured\_in\_E}/U_{ave}$) in time inside the feed channels at three levels: middle of the channel (Z2), next to the window of the flow cell (Z1) and close to the membrane (Z3). Circles inside the box represent the average of data and continuous horizontal lines the median. The filled circles outside the box represent the outliers.

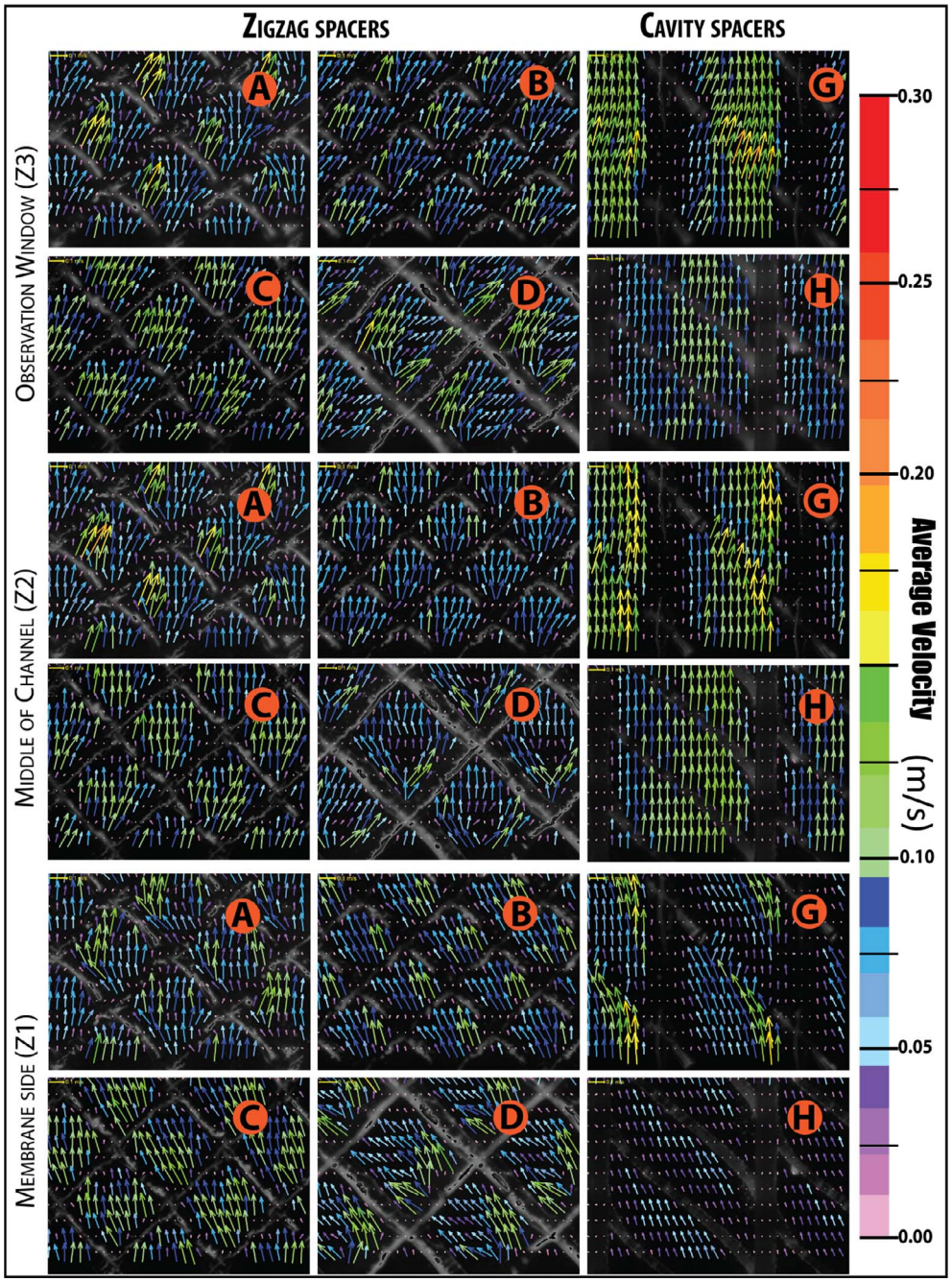

Fig. 7. Time-averaged velocity fields for spacers at three channel heights: Z1, Z2, and Z3 for an average velocity of approximately 0.1 m/s.

studied zigzag spacers (Fig. 10). This could indicate a notable flow mixing in zigzag spacers occurs at Reynolds numbers around 60–100. However, these changes in the flow patterns don not necessarily indicate mixing. That could only be assessed by 3D movies of the flow or by evaluating other factors some of which is mentioned by Liang et al. [38]. Fig. 10 illustrates the variation of velocity in time with an increasing Reynolds number for point E, the middle of the mesh. The low variation of velocity at low Reynolds numbers ($Re_h < 30$) indicates the existence of steady flow in these conditions and starting the unsteadiness at $Re_h > 30$. The obtained results for the zigzag spacers are in agreement with the common belief that spacers induce flow instabilities at low Reynolds number and with results from previous studies [13]. Koutsou et al. [13] found that a transition to unsteady flow occurs at relatively low Reynolds numbers (Re = 35–45).

Additionally, there is a variation of velocity at $Re_h > 90$, which indicates a significant increase in flow instabilities in the channels. This is agreement with practical situations in which the reverse osmosis membranes are operated at $100 < Re_h < 300$.

Variation of velocities from the mean becomes significant at Reynolds numbers around 90. The difference between the velocity at the membrane side (Z1) with the velocity at the middle of the channel (Z2) and the observation window (Z3) at $30 < Re_h < 65$ might be due to the existence of preferential flow at one side of the membrane at this range of Reynolds number in the zigzag spacers.

In cavity spacers, the difference in velocity between two measured sequential Reynolds numbers can be noticed more easily by considering the velocity at the membrane side (Z1), on which transverse filaments are placed. This difference starts at $Re_h = 60$.

In conclusion, the flow with spacers and conditions used in this study can be characterized as a laminar-steady flow for $Re_h < 30$ and laminar-unsteady for $Re_h > 90$. The flow is laminar because Reynolds numbers are much lower than the values for turbulent flow conditions

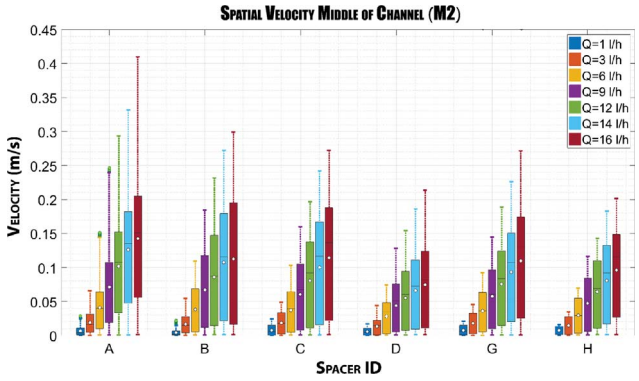

Fig. 8. Development of averaged spatial velocity for the whole field of view at the middle of the channel. Each plotted box corresponds to the measured velocity at a specific flow rate.

(Re_h > 4000) and even transition conditions (2000 < Re_h < 4000). The flow becomes unsteady at Re_h > 90 because the velocity variation in time become significantly higher than the temporal velocity variation at Re_h < 90.

4. Conclusion

In this study, we experimentally evaluated the performance of spacers with different configurations by determining their pressure drop, flow conditions, and local velocity profiles. The pressure drop increased by increasing the Reynolds number for a constant geometry of spacer and feed channel. The pressure drop increased by decreasing the channel height in zigzag spacers and by increasing the thickness of transverse filaments in cavity spacers. The results from Particle Image Velocimetry (PIV) showed that the variation of velocity increases by the increase in the channel height in the zigzag spacers and the increase of the transverse filament's thickness in the cavity spacers.

As expected, the averaged value of measured velocity, the variation of velocity, and the pressure drop increased by increasing the flow rate with each spacer.

Curves of the friction factor against the Reynolds number had the shape of a decreasing power function. The transition region from steady to unsteady flow was the moment that the incline of friction factor changed from steep to slight, i.e. at Reynolds number greater than 30. The flow in zigzag spacers was in a straight line from inlet to outlet at Re_h < 30, but it was along filaments at each depth at higher Reynolds numbers. At 30 < Re_h < 90, the flow in zigzag spacers was along the spacers' filaments at the membrane sides (Z1, Z3) but in a straight line from the inlet to outlet in the middle of the channel. At Re_h > 90, the flow pattern in the middle of the channel (Z2) was the same as it is described by Willems et al. [25], i.e. the flow was a mixture of flow patterns at the top part of flow channel (Z3) and the rear part of the flow channel (Z1).

The velocity variation over time, which indicates the degree of unsteadiness, was very subtle at Re_h < 30 and considerable at Re_h > 90. These values are in agreement with respectively the common belief that spacers induce flow instability and the practical operation of reverse osmosis membrane. It must be emphasized that such a clear demonstration of flow instability was not found in previous studies related to spacer-filled channel.

These results can be used to evaluate configurations and geometries of feed spacers. The high-resolution velocity profiles in our study could be exploited as a testing tool for numerical studies. While our results provide a reasonable estimation of the velocity maps at the X- and Y-direction of the flow asynchronously at three different heights (Z1, Z2, and Z3) of a channel, further experimental investigations would be required to quantify the effect of velocity in the Z-direction simultaneously with that of the XY-plane.

Acknowledgements

This research was made possible by the financial support of Vitens Water Company, which we gratefully acknowledge. We would also like to thank Mr. Martin Verebes from DelStar Technologies Inc. for providing us with the required feed spacers and Dr. Cristian Picioreanu for his help in analyzing some of our data. We also wish to thank Mr. James Kidwell and Mr. Andreas Bergen from Conwed Plastics N.V. for their help.

Appendix A. Supplementary material

Supplementary data associated with this article can be found, in the online version, at http://dx.doi.org/10.1016/j.seppur.2018.01.022.

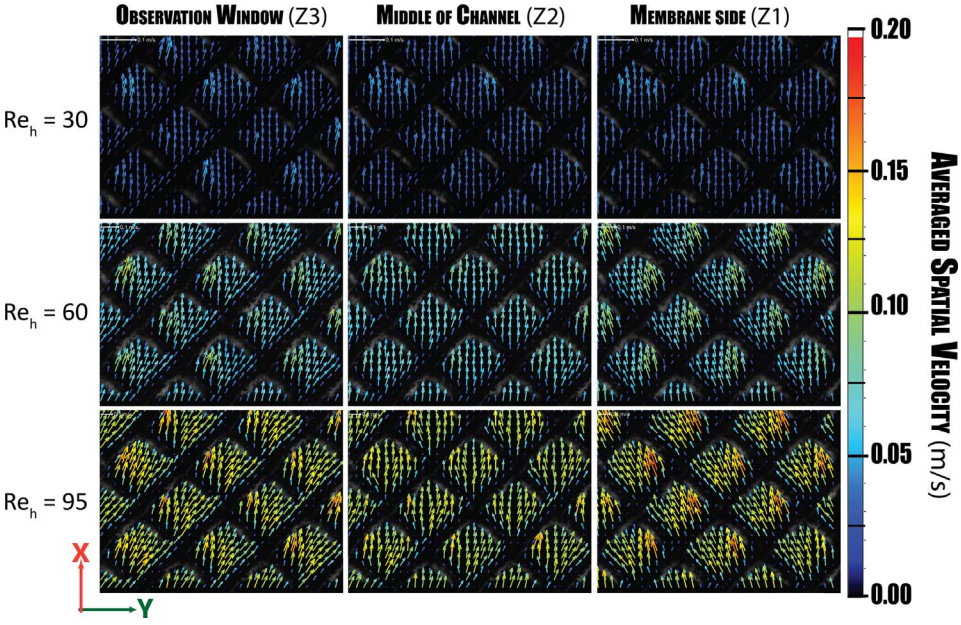

Fig. 9. Development of flow pattern in spacer B for Reynolds number of 31, 61, and 94 at three channel heights. The corresponding friction factor curve has a break point in 31 < Re < 94 from descent steep incline to descent slight incline.

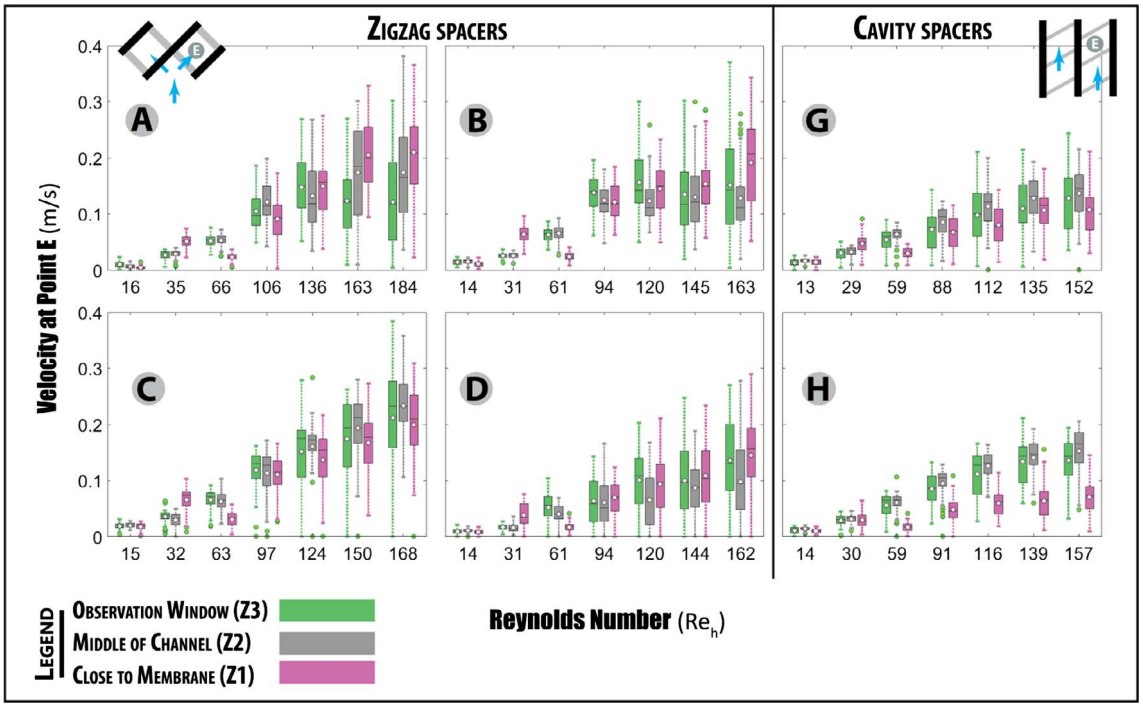

Fig. 10. Variation of velocity in time for point E in the middle of the mesh.

References

[1] L.B. de Chazournes, Fresh Water in International Law, 2013.
[2] C. Wong, Williams, CE, Pittock, J, Collier, U and Schelle P, World's top 10 rivers at risk, in: WWF for living planet, WWF Global Freshwater Programme, Gland, Switzerland., March 2007.
[3] DesalData, Forecast – DesalData, in, 2015.
[4] CONWED.Global.Netting.Solutions, Pressure drop, membrane damage and bio-fouling, the primary challenges in Reverse Osmosis, in: C. Plastics (Ed.) Reverse Osmosis series, Conwed Plastics.
[5] W.G.J. van der Meer, J.C. van Dijk, Theoretical optimization of spiral-wound and capillary nanofiltration modules, in: Desalination Workshop on Membranes, in: Drinking Water Production Technical Innovations and Health Aspects, 1997, pp. 129–146.
[6] G. Schock, A. Miquel, Mass transfer and pressure loss in spiral wound modules, Desalination 64 (1987) 339–352.
[7] A.R. Da Costa, A.G. Fane, Net-Type Spacers: Effect of Configuration on Fluid Flow Path and Ultrafiltration Flux, Industrial & Engineering Chemistry Research, American Chemical Society, 1994, pp. 1845–1851.
[8] C.C. Zimmerer, V. Kottke, Effects of spacer geometry on pressure drop, mass transfer, mixing behavior, and residence time distribution, Desalination 104 (1996) 129–134.
[9] V. Geraldes, V. Semião, M.N. de Pinho, Flow management in nanofiltration spiral wound modules with ladder-type spacers, J. Membr. Sci. 203 (2002) 87–102.
[10] V. Geraldes, V. Semião, M.N. de Pinho, The effect of the ladder-type spacers configuration in NF spiral-wound modules on the concentration boundary layers disruption, Desalination 146 (2002) 187–194.
[11] V. Geraldes, V. Semião, M. Norberta Pinho, Hydrodynamics and concentration polarization in NF/RO spiral-wound modules with ladder-type spacers, Desalination 157 (2003) 395–402.
[12] J.L.C. Santos, V. Geraldes, S. Velizarov, J.G. Crespo, Investigation of flow patterns and mass transfer in membrane module channels filled with flow-aligned spacers using computational fluid dynamics (CFD), J. Membr. Sci. 305 (2007) 103–117.
[13] C.P. Koutsou, S.G. Yiantsios, A.J. Karabelas, Direct numerical simulation of flow in spacer-filled channels: effect of spacer geometrical characteristics, J. Membr. Sci. 291 (2007) 53–69.
[14] C.P. Koutsou, S.G. Yiantsios, A.J. Karabelas, Numerical simulation of the flow in a plane-channel containing a periodic array of cylindrical turbulence promoters, J. Membr. Sci. 231 (2004) 81–90.
[15] F. Li, G.W. Meindersma, A.B. de Haan, T. Reith, Optimization of non-woven spacers by CFD and validation by experiments, Desalination 146 (2002) 209–212.
[16] F. Li, W. Meindersma, A.B. de Haan, T. Reith, Novel spacers for mass transfer enhancement in membrane separations, J. Membr. Sci. 253 (2005) 1–12.
[17] F. Li, W. Meindersma, A.B. de Haan, T. Reith, Optimization of commercial net spacers in spiral wound membrane modules, J. Membr. Sci. 208 (2002) 289–302.
[18] J. Schwinge, P.R. Neal, D.E. Wiley, D.F. Fletcher, A.G. Fane, Spiral wound modules and spacers: review and analysis, in: J. Membr. Sci., Membrane Engineering Special Issue, 2004, pp. 129–153.
[19] G.A. Fimbres-Weihs, D.E. Wiley, Review of 3D CFD modeling of flow and mass transfer in narrow spacer-filled channels in membrane modules, in: Chemical Engineering and Processing: Process Intensification, Process Intensification on Intensified Transport by Complex Geometries, 2010, pp. 759–781.
[20] A.R. Da Costa, A.G. Fane, C.J.D. Fell, A.C.M. Franken, Optimal channel spacer design for ultrafiltration, J. Membr. Sci. 62 (1991) 275–291.
[21] A.R. Da Costa, A.G. Fane, D.E. Wiley, Spacer characterization and pressure drop modelling in spacer-filled channels for ultrafiltration, J. Membr. Sci. 87 (1994) 79–98.
[22] P.R. Neal, H. Li, A.G. Fane, D.E. Wiley, The effect of filament orientation on critical flux and particle deposition in spacer-filled channels, J. Membr. Sci. 214 (2003) 165–178.
[23] S.S. Bucs, A.I. Radu, V. Lavric, J.S. Vrouwenvelder, C. Picioreanu, Effect of different commercial feed spacers on biofouling of reverse osmosis membrane systems: a numerical study, Desalination 343 (2014) 26–37.
[24] A.I. Radu, M.S.H. van Steen, J.S. Vrouwenvelder, M.C.M. van Loosdrecht, C. Picioreanu, Spacer geometry and particle deposition in spiral wound membrane feed channels, Water Res. 64 (2014) 160–176.
[25] P. Willems, N.G. Deen, A.J.B. Kemperman, R.G.H. Lammertink, M. Wessling, M. van Sint Annaland, J.A.M. Kuipers, W.G.J. van der Meer, Use of particle imaging velocimetry to measure liquid velocity profiles in liquid and liquid/gas flows through spacer filled channels, J. Membr. Sci. 362 (2010) 143–153.
[26] C. Gaucher, P. Legentilhomme, P. Jaouen, J. Comiti, J. Pruvost, Hydrodynamics study in a plane ultrafiltration module using an electrochemical method and particle image velocimetry visualization, Experiments in Fluids, Springer-Verlag, 2002, pp. 283–293.
[27] M. Gimmelshtein, R. Semiat, Investigation of flow next to membrane walls, J. Membr. Sci. 264 (2005) 137–150.
[28] A.H. Haidari, S.G.J. Heijman, W.G.J. van der Meer, Visualization of hydraulic conditions inside the feed channel of Reverse Osmosis: a practical comparison of velocity between empty and spacer-filled channel, Water Res. 106 (2016) 232–241.
[29] P. Hickey, Gooding, CH, Proceedings of Sixth International Conference on Pervaporation Processes in the Chemical Industry in: B.M. Corporation (Ed.) Pervaporation processes in the chemical industry, Bakish Materials Corporation, Ottawa, Canada, 1992, pp. 153–169.
[30] R.B. Bird, W.E. Stewart, E.N. Lightfoot, Transport Phenomena, Wiley, 2007.
[31] E. Pellerin, E. Michelitsch, K. Darcovich, S. Lin, C.M. Tam, Turbulent transport in membrane modules by CFD simulation in two dimensions, J. Membr. Sci. 100 (1995) 139–153.
[32] G.A. Fimbres-Weihs, D.E. Wiley, Numerical study of mass transfer in three-dimensional spacer-filled narrow channels with steady flow, J. Membr. Sci. 306 (2007) 228–243.
[33] S.K. In, N.C. Ho, The effect of turbulence promoters on mass transfer-numerical analysis and flow visualization, Int. J. Heat Mass Transfer 25 (1982) 1167–1181.
[34] B. McKeon, G. Comte-Bellot, J. Foss, J. Westerweel, F. Scarano, C. Tropea, J. Meyers, J. Lee, A. Cavone, R. Schodl, M. Koochesfahani, Y. Andreopoulos, W. Dahm, J. Mullin, J. Wallace, P. Vukoslavčević, S. Morris, E. Pardyjak, A. Cuerva, Velocity, Vorticity, and Mach Number, in: C. Tropea, A.L. Yarin, J.F. Foss (Eds.), Springer Handbook of Experimental Fluid Mechanics, Springer, Berlin Heidelberg, Berlin, Heidelberg, 2007, pp. 215–471.

[35] H. Klank, G. Goranović, J.P. Kutter, H. Gjelstrup, J. Michelsen, C.H. Westergaard, PIV measurements in a microfluidic 3D-sheathing structure with three-dimensional flow behaviour, J. Micromech. Microeng. 12 (2002) 862.
[36] J. Schwinge, D.E. Wiley, A.G. Fane, Novel spacer design improves observed flux, J. Membr. Sci. 229 (2004) 53–61.
[37] S.K. Karode, A. Kumar, Flow visualization through spacer filled channels by computational fluid dynamics I.: Pressure drop and shear rate calculations for flat sheet geometry, J. Membr. Sci. 193 (2001) 69–84.
[38] Y.Y. Liang, G.A. Fimbres Weihs, D.E. Wiley, CFD modelling of electro-osmotic permeate flux enhancement in spacer-filled membrane channels, J. Membr. Sci. 507 (2016) 107–118.